Multifunctional nanoparticles by coordinative self-assembly of His-tagged units with metal-organic frameworks

Journal:	*Journal of the American Chemical Society*
Manuscript ID	ja-2016-11934z.R1
Manuscript Type:	Article
Date Submitted by the Author:	07-Jan-2017
Complete List of Authors:	Röder, Ruth; Ludwig-Maximilians-University Munich, Department of Pharmacy Preiß, Tobias; Ludwig-Maximilians-Universitat Munchen Hirschle, Patrick; Ludwig-Maximilians-Universität München, Department of Chemistry Steinborn, Benjamin; Ludwig-Maximilians-Universitat Munchen, Pharmacy Zimpel, Andreas; Ludwig-Maximilians-Universitat Munchen Hoehn, Miriam; LMU, Rädler, Joachim; Ludwig-Maximilians-University Munich Lehrstuhl für Biophysik / soft condensed matter, CeNS & Physik Department,Geschwister-Scholl-Platz 1, D-80539 München, Germany Bein, Thomas; Ludwig-Maximilians-Universität München, Chemistry and Biochemistry Wagner, Ernst; LMU Munich, Department of Pharmacy Wuttke, Stefan; University of Munich, Chemisry Lächelt, Ulrich; Ludwig-Maximilians-University Munich, Department of Pharmacy

Multifunctional nanoparticles by coordinative self-assembly of His-tagged units with metal-organic frameworks

Ruth Röder,[†] Tobias Preiß,[‡] Patrick Hirschle,[§] Benjamin Steinborn,[†] Andreas Zimpel,[§] Miriam Höhn,[†] Joachim O. Rädler,[‡] Thomas Bein,[§] Ernst Wagner,[†] Stefan Wuttke,[§]* and Ulrich Lächelt[†]*

[†]Pharmaceutical Biotechnology, Center for System-Based Drug Research, and Center for NanoScience (CeNS), LMU Munich, Germany.

[‡]Department of Physics, and Center for NanoScience (CeNS), LMU Munich, Germany.

[§]Department of Chemistry and Center for NanoScience (CeNS), LMU Munich, Germany.

Histidine-tag, Metal-organic framework (MOF), Nanoparticle, Protein delivery, Surface functionalization.

ABSTRACT: Self-assembly of individual units into multicomponent complexes is a powerful approach for the generation of functional super-structures. We present the coordinative interaction of oligohistidine-tags (His-tags) with metal-organic framework nanoparticles (MOF NPs). By this novel concept, different molecular units can be anchored on the outer surface of MOF NPs in a self-assembly process generating multifunctional nanosystems. The article focuses on two main objectives: first, the detailed investigation of the assembly process and fundamental establishment of the novel functionalization concept; and second, its subsequent use for the development of biomacromolecule (e.g. peptides and proteins) delivery vehicles. Three exemplary MOF structures, MIL-88A, HKUST-1 and Zr-*fum*, based on different metal components, were selected for the external binding of various His-tagged synthetic peptides and recombinant or chemically H_6-modified proteins. Evidence for simultaneous assembly of different functional units with Zr-*fum* MOF NPs as well as their successful transport into living cells illustrate the promising potential of the self-assembly approach for the generation of multifunctional NPs and future biological applications. Taking the high number of possible MOF NPs and different functional units into account, the reported functionalization approach opens great flexibility for the targeted synthesis of multifunctional NPs for specific purposes.

INTRODUCTION

Nanoparticles (NPs) that combine different functional domains are of high interest for various scientific disciplines requiring multifunctionality at the nanoscale. The controlled manipulation of the external surface of NPs is of paramount importance as it defines the interface between the NP and its surroundings and strongly determines the overall performance of the NP especially in biologic environments[1,2]. Researchers have shown that surface functionalization is a powerful tool for the creation of programmable NP interfaces. In this respect, the self-assembly of the functional units onto the NPs surface appears as a powerful approach because it would ensure a defined arrangement of these units without any guidance from an external source. Examples of self-assembly processes used for the generation of multifunctional colloidal NPs are micelle, liposome or polymerosome formation of amphiphilic compounds[3-6] and cyclodextrin-adamantane host-guest interactions[7,8]. Especially for biomedical applications, multifunctional NPs that interact with biological systems at the molecular level and perform tasks within cellular systems are in great demand[9,10]. The intracellular delivery of biomacromolecules, such as peptides and proteins, represents a particularly challenging task. Several different barriers have to be overcome, including cellular uptake, endosomal escape, intracellular trafficking and cargo release[11,12]. The heterogeneity of this compound class (hydrophilicity, charge, functional groups) hampers the development of universal delivery platforms. For this reason, nanocarriers with a functionalization mode, which is independent from the individual properties of the functional units, would be advantageous.

Here, we present the coordinative interaction of oligohistidine-tags with metal-organic frameworks (MOFs) as a novel external functionalization concept for MOF NPs based on a self-assembly process. MOFs are a class of materials synthesized of inorganic building units, metal ions or metal oxide clusters, which are coordinatively connected by organic linkers to create porous three-dimensional frameworks (Figure 1a)[13]. Their crystallinity, chemically functionalizable pores and potential systematic structural variation are some factors amongst others that allow to precisely design these materials for particular purposes[14,15]. Regarding biomedical applications, the

hybrid MOF nature provides the advantageous potential of degradability and disintegration into the low molecular weight components which can be eliminated from the body[16-19]. Different research groups have already reported pioneering examples of MOF NPs as transport vehicles for the delivery of biologically active molecules[16,20-27]. Here the combination of MOF high surface area for high drug loading and the possibility to engineer the internal surface to control MOF scaffold-guest interaction was used to optimize the nanocarrier performance[28]. Even, biomacromolecules such as proteins, DNA or enzymes could be recently encapsulated into MOFs[29,30] or the MOF scaffold itself could be used as a part of the therapeutic principle[31-34]. Therefore, combining the rich and versatile bulk chemistry of MOF materials with controlled and programmable NP interfaces may lead to novel multifunctional nanosystems[35-40]. Our concept uses the interaction between Lewis bases, such as the imidazole function of histidine and coordinatively unsaturated metal sites (CUS) present on the external surface of MOF NPs (Figure 1b) to self-assemble different functional units (Figure 1c).

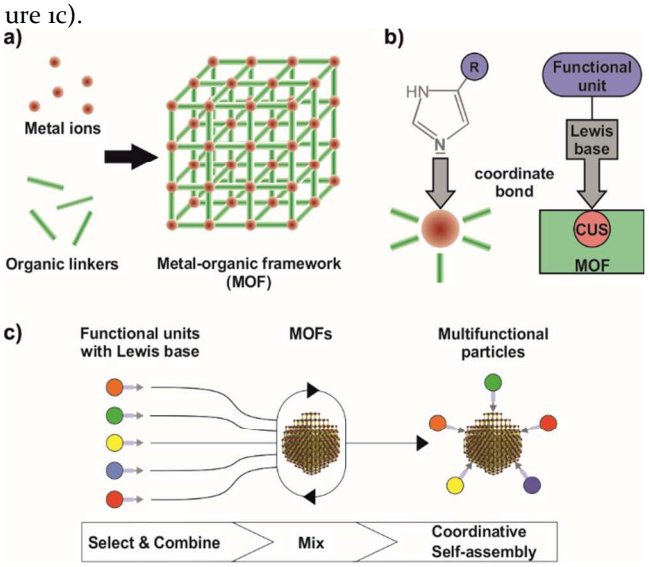

Figure 1. Illustration of coordinative self-assembly of His-tagged molecules with MOF NPs: a) molecular composition of MOFs; b) coordinative bond between the imidazole group of histidines acting as Lewis base and coordinatively unsaturated metal sites (CUS) acting as Lewis acid; c) multifunctional MOF NPs generated by coordinative attachment of different functional units via self-assembly.

The exemplary set of (oligohistidine-tag) functional units used in this study is summarized in Table 1. Since His-tags can be readily integrated into peptides or proteins by synthetic, recombinant or bioconjugation techniques, they appear to be ideal connectors to create a versatile inorganic/bioorganic interface at the MOF NPs' surface. The same interaction (Figure 1b) is routinely used for the purification of recombinant proteins by immobilized metal ion chromatography[41,42]. Applicability of the coordinative His-tag interactions for intracellular delivery of proteins has been demonstrated before by using conjugates of nitrilo-triacetic acid derivatives and cell-penetrating peptides[43,44], polymers[45] or silica NPs[46]. In these approaches, the delivery platforms and vehicles were synthetically modified with separate metal-chelators. Since the metal-sites already are an integral part of the coordinative MOF structure, the external secondary modification via coordinate bonds in the presented approach of 'self-assembling multifunctional coordination particles' (SAMCOPs) is considered a powerful tool for the combinatorial and stoichiometric generation of functional MOFs.

Table 1. His-tagged functional units used for the assembly with MOF NPs.

Code	Sequence[a] / Description	Function
H_6-Acr	Acridine-PEG_{28}-H_6NH_2	Photometric detection
$H_{0/3/6}$-Acr	Acridine-STOTDA-$H_{0/3/6}$	
$H_{0/3/6}$-FITC	FITC-STOTDA-H_6	
H_6-A647N	ATTO647N-PEG_{12}-H_6NH_2	Fluorescence detection
H_6-CF	Carboxyfluorescein-PEG_{12}-H_6NH_2	
H_6-GFP	Recombinant eGFP (H_6-Tag)	Model proteins
H_6-Tf*	Transferrin conjugated with H_6-PEG_{36} and ATTO647N	
H_6-Bak	H_6-GGQVGRQLAIIGDDINR$_{NH_2}$	Apoptotic peptides
H_6-Bad	H_6-GNLWAAQRYGRELRRMSDEFVD$_{NH_2}$	
H_6-KLK	H_6-GGKLAKLAKKLAKLAK$_{NH_2}$	
H_6-CytC	Cytochrome C conjugated with H_6	Apoptotic protein

[a] Peptide sequences are indicated from N- to C-terminus using the one-letter code for α-amino acids (H_n, n = number of histidines); * ATTO647N label.

RESULTS AND DISCUSSION

Selection and characterization of MOF NPs. A set of three exemplary MOF structures, MIL-88A (Fe^{3+}/fumaric acid)[16], HKUST-1 (Cu^{2+}/trimesic acid)[47] and Zr-*fum* (Zr^{4+}/fumaric acid)[48,49] was selected for testing the assembly strategy. HKUST-1 was chosen based on the high His-tag affinity toward chelated Cu^{2+}, which even exceeds affinity toward Ni^{2+} and Co^{2+} [50,51]. MIL-88A and Zr-*fum* represent well established MOFs with potential for biomedical applications[16,18]. Although Ni^{2+}, Co^{2+} and Zn^{2+} are known to have high affinity to His-tags[50,51], we did not include them in the study due to the expected cytotoxicity of Ni^{2+} and Co^{2+} MOFs and the low stability of Zn-based MOFs in aqueous media. Together, the set covers a range of well-established MOF species with individual material characteristics and each based on a different di-, tri- or tetravalent metal component with expected different His-tag binding capacities.

The quality of the MOF NPs used in this study was ensured by applying multiple complementary characterization techniques: scanning electron microscopy (SEM, Figures S10-S15), dynamic light scattering (DLS, Figures

S1-S2, Table S2), X-ray diffraction (XRD, Figures S3-S5), thermogravimetric analysis (TGA, Figures S6-S8) and nitrogen sorption measurements providing the surface area (Figure S9, Table S3). Powder XRD patterns were determined for all MOF NP species (Figures S3-S5). The diffractograms were used to verify the successful synthesis of the MOF species as well as to show the high crystallinity of the Zr-*fum* and HKUST-1 NPs. It should be noted that the poor crystallinity of the MIL-88A NPs are expected and have been frequently reported and discussed in the literature[16,52-55]. At the same time XRD was used to prove the stability of the three MOFs under the later used conditions (Figures S3-S5). For additional bulk characterization, all NP species were examined with both nitrogen sorption experiments (Figure S9, Table S3) and TGA (Figures S6-S8). The microporosity of all three NP species ranging from 0.6 up to 1.5 nm was confirmed and the BET surface area yielded typical results[16,47-49]. Thus, we have successfully synthesized the MIL-88A, HKUST-1 and Zr-*fum* MOF structures with their expected bulk properties.

In order to characterize their corresponding NP properties a combination of two techniques were used: particle size distributions were determined via scanning electron microscopy (SEM, Figures S10-S15) for the dried species and, more importantly, for the dispersed species via dynamic light scattering (DLS, Figures S1-S2, Table S2). For Zr-*fum*, SEM measurements resulted in a diameter of (84 ± 7) nm for the dried particles. The corresponding z-average diameter measured via DLS in water was determined at (182 ± 4) nm with a polydispersity index (PDI) of 0.205. This deviation towards larger diameters is to some extent expected, since DLS provides the hydrodynamic diameter of the particles and is influenced amongst others by particle-solvent interactions and aggregation[56,57]. The other MOFs behave similarly: DLS experiments resulted in an average intensity based diameter of (191 ± 1) nm (PDI = 0.130) for MIL-88A and (530 ± 27) nm (PDI = 0.290) for HKUST-1 with the corresponding dried particle size distributions of (61 ± 7) nm for MIL-88A and for HKUST-1 (177± 39) nm. We suppose that the main reason for the larger NP diameters determined using DLS is due to the fact that the MOF samples reveal agglomeration behavior in solution[56].

Photometrical analysis of His-tag binding to MOF NPs. The binding of different His-tag model peptides (e.g. H_n-Acr, H_n-FITC, H_6-A647N) to MIL-88A, HKUST-1 and Zr-*fum* in HEPES buffered glucose (HBG) at pH 7.4 was determined by the detection of residual free peptide in the supernatant after incubation and centrifugation of the MOF suspensions (Figures 2a, 2b, 2d, 3, S17, S19, Scheme S1). An exemplary movie demonstrating the binding of H_6-A647N to HKUST-1 MOF NPs visualized by decoloration of the supernatant after centrifugation is provided as supporting material for download. The exclusive reduction of H_6-Acr (in contrast to A_6-Acr) in the supernatant, illustrated by the discrete diminution of the H_6-Acr peak in the RP-HPLC chromatograms, represents qualitative evidence for the histidine-dependent interaction with all three investigated MOF species (Figure 2b). The peptide-specific binding was also verified by zeta potential measurements (Figure 2c) showing a significant shift towards neutrality caused by the His-tag containing derivatives only. Quantitative determination of binding as a function of histidine residues, i.e. number of Lewis base units (H_o, H_3, H_6) was carried out by photometric quantification of residual free peptide using a UV-photometer (Figure 2d). The amount of bound H_3- and H_6-peptides increased with increasing amounts of MOFs, but binding of the H_o derivative, corresponding to no histidine residue, was generally negligible. Notably, in case of all three MOFs significantly higher peptide binding was observed with higher number of histidines (H_o vs. H_3 and H_3 vs. H_6).

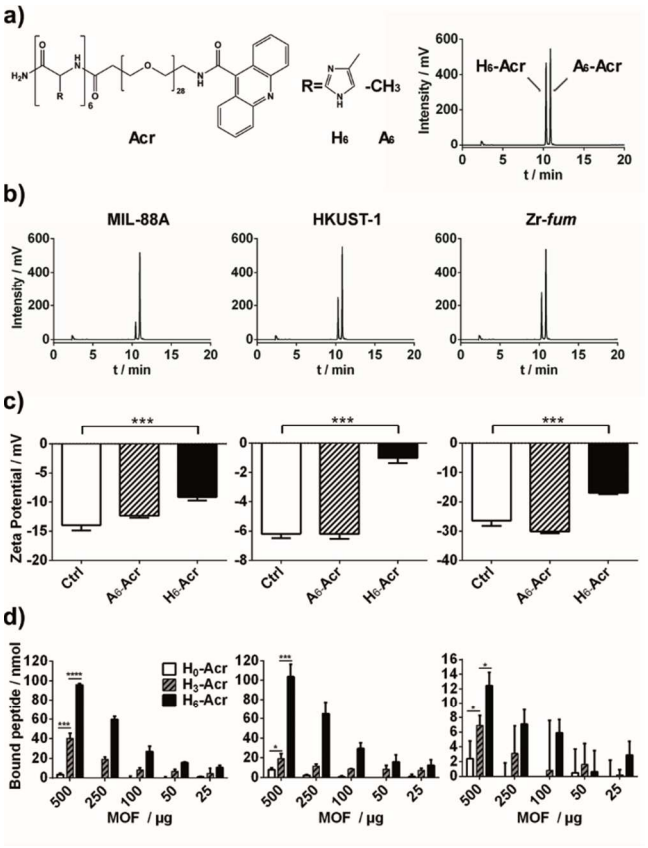

Figure 2. Acridine (Acr) peptide binding to MIL-88A (left), HKUST-1 (middle) and Zr-*fum* (right) particles in HEPES buffered glucose (HBG) at pH 7.4. a) Chemical structure and control chromatogram of model compounds H_6-Acr, A_6-Acr. b) Peptide binding (H_6 vs. A_6) by detection of reduced free peptides in the supernatant (RP-HPLC, λ=360 nm). c) Effect of peptide binding on zeta potential. d) Quantitative determination of bound peptides H_o (white), H_3 (pattern), H_6 (black) as difference to photometrically quantified free peptides in the supernatant (λ=360 nm) using a UV-photometer. Please note that the scaling of y-axes is accommodated to the different binding capacities: 0-120 nmol peptide in case of MIL-88A and HKUST-1, 0-16 nmol peptide in case of Zr-*fum*.

This correlation was additionally confirmed for Zr-*fum* via fluorescence spectroscopy by using FITC labeled peptides ($H_{o/3/6}$-FITC) (Figure S19). Excessive addition of imidazole decreased binding of H_6-FITC to levels of H_o-FITC, suggesting competition of histidine and free imidazole for coordinative interaction with the MOF surface,

similar to the elution of His-tagged proteins from a nickel-column in immobilized-metal ion chromatography purifications. Comparing H_6-tag binding to 500 µg MOF NPs, HKUST-1 achieved the highest binding (104 nmol), followed by MIL-88A (96 nmol) and Zr-*fum* (12 nmol) which is consistent with reported metal ion affinities (Cu^{2+} > Fe^{3+}, Zr^{4+}) for His-tags[41]. A time course experiment (Figure 3b) revealed stable association of Zr-*fum*/H_6-A647N for 24 h at pH 7.4 and rapid partial (pH 5) or complete (pH 3) release upon acidification. This is consistent with the hypothesis of unprotonated histidines acting as Lewis base and being responsible for binding (Figure 2a). We suggest that the incomplete detachment at pH 5 is caused by a lowered pK_a of the imidazole group due to metal ion binding[58] and an equilibrium between protons and metal ions competing for histidine interactions.

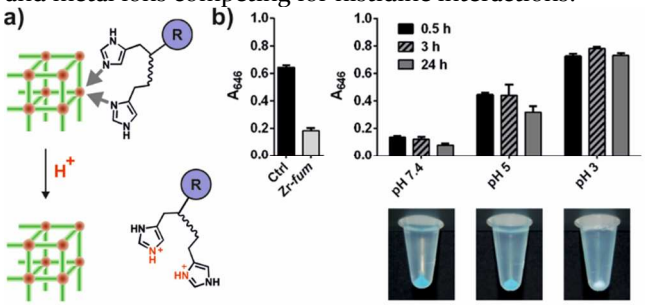

Figure 3. pH dependent stability of H_6-tag binding to Zr-*fum* NPs. a) Schematic illustration of acidic detachment due to histidine protonation. b) Experimental data obtained by photometric determination (λ=646 nm) of free H_6-A647N in the supernatant after centrifugation. Left: Zr-*fum* NPs were loaded with H_6-A647N at pH 7.4 for 15 min, centrifuged and the supernatant was analyzed; Ctrl illustrates absorbance of free peptide in a sample without MOF NPs. Right: MOF NP suspensions were acidified to a defined pH and incubated for indicated times before centrifugation and analysis of the supernatant. Reaction tubes below show the MOF pellets of the same samples after 24 h at pH 7.4 (left), pH 5 (middle), pH 3 (right) and centrifugation; decoloration of the pellet due to acidic H_6-A647N detachment at pH 3 can be observed.

Fluorescence Correlation Spectroscopy (FCS). Using FCS the binding of fluorescently labeled H_6-tags to MOF particles was measured at low concentrations with single-molecule sensitivity (Figure 4, S18). Figure 4 (upper left) and Figure S18 show a significant increase in the autocorrelation amplitude after addition of all three MOF species, indicating a reduction of the H_6-tag number concentration most likely due to multiple binding to MOF NPs. In case of MIL-88A and HKUST-1 (Figure S18), however, no change in the characteristic correlation decay time could be detected. We attribute this to the known phenomenon of MOF induced fluorescence quenching[59,60] as well as rather large effective particle sizes, in particular of HKUST-1, resulting from aggregation, which both can cause a decline of detectable tags after binding. For Zr-*fum* NPs several key observations could be made (Figure 4). Free H_6-tags (grey) showed fast single molecule diffusion prior to NP addition (Figure 4, lower left). After addition of Zr-*fum* NPs at pH 7.4 (orange) the collective diffusion was shifted towards higher diffusion times revealing H_6-tag binding to Zr-*fum* NPs. Following acidification (green) the diffusion rate increased relative to the pH 7.4 measurement indicating partial detachment of His-tags from the MOF NP surface, due to the protonation of histidines.

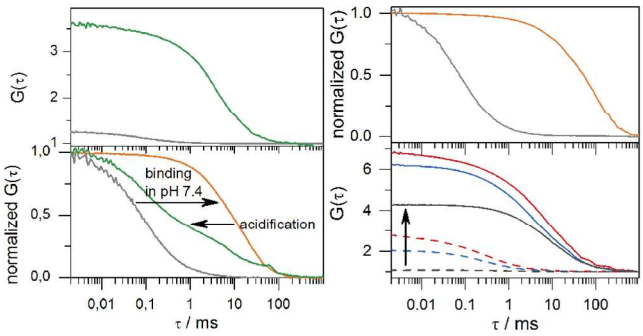

Figure 4. Investigation of Zr-*fum*/H_6-A647N interaction by fluorescence correlation spectroscopy (FCS). Upper left: FCS time correlation functions of H_6-A647N before (grey) and after Zr-*fum* NP addition (green). Lower left: Normalized time correlation functions of binding of H_6-A647N at pH 7.4 (orange) and release upon acidification (green); free H_6-A647N (grey). Upper right: Normalized time correlation functions of measurements in DMEM (10 % FBS) of free H_6-A647N (grey) and Zr-*fum*/H_6-A647N (orange). Lower right: fluorescence cross correlation spectroscopy (FCCS) measurements of H_6-GFP (blue) and H_6-Tf* (red) in HBG pH 7.4 before (dotted) and after (solid) Zr-*fum* addition. Cross correlation before (dotted grey) and after (solid grey) Zr-*fum* addition.

Importantly, H_6-tag association with Zr-*fum* NPs remained stable after dilution in DMEM medium containing 10 % fetal bovine serum (FBS), confirming the suitability for use under cell culture conditions (Figure 4, upper right). Finally, two His-tagged proteins with distinct fluorescence spectra (recombinant eGFP with genetically encoded His-tag: H_6-GFP, and human transferrin chemically conjugated with a H_6-tag and Atto647N label: H_6-Tf*) were used for fluorescence cross correlation spectroscopy (FCCS) measurements to investigate simultaneous binding of both entities to single particles (Figure 4, lower right). In a solution containing equimolar amounts of both proteins the cross correlation showed high coincidence of H_6-GFP and H_6-Tf* after addition of Zr-*fum* NPs (solid grey), which demonstrated binding of different His-tagged proteins to the same Zr-*fum* particles. Importantly both FCS and FCCS experiments revealed the colloidal stability of the MOF NPs. Additionally, the framework stability of the particles prior to and after functionalization under aqueous conditions was investigated by XRD measurements (Figures S3-S5). The experiments showed the nearly unchanged crystallinity of all samples under each tested condition. In case of Zr-*fum* MOF NPs this was also confirmed by SEM and DLS measurements, exhibiting no observable change in morphology of dried particles and moderate effect on hydrodynamic size of dispersed particles upon modification with H_6-Acr in HBG pH 7.4 (Figures S2 and S16).

Cellular uptake of model peptides and proteins with MOF NPs. To assess the potential of MOF NPs to mediate cellular internalization of biomacromolecules, H_6-Carboxyfluorescein (H_6-CF), recombinant eGFP with genetically encoded His-tag (H_6-GFP) and chemically His-tagged and ATTo647N labeled human transferrin (H_6-Tf*) were used as fluorescent model compounds. Based on the photometrical analysis of His-tag binding to the three MOF species (Figure 2d), the His-tagged functional units were used at a ratio of 10 nmol H_6-tag per 1 mg MOF which is considerably below the determined binding capacities of 192 nmol/mg MIL88A, 208 nmol/mg HKUST-1 and 24 nmol/mg Zr-*fum*. First, cell viability of HeLa cells after incubation with different amounts of all three MOF NPs and different His-tags for 48 h was evaluated by MTT-assay (Figure S20). MIL-88A, Zr-*fum*, and the tested His-tags H_6-CF, H_6-GFP and H_6-Tf, were very well tolerated. HKUST-1 exhibited considerable cytotoxicity, which could be avoided by shortening the incubation time with cells to 2 h followed by medium exchange, which deleted observable effects on metabolic activity at the endpoint evaluation after 48 h (Figure S20b). Next, cellular uptake of the different MOF NPs after functionalization with the H_6-tagged fluorescent dye H_6-CF or H_6-GFP was investigated. For prefunctionalization by coordinative self-assembly, His-tags and MOF NPs were mixed at a final concentration of 10 µM H_6-tag and 1 mg/ml MOF in HBG buffer (ratio of 10 nmol H_6-tag per 1 mg MOF) and incubated for 15 min at room temperature. Cells were then incubated with the different functionalized MOF NPs for 24 h in medium at a concentration of 0.1 mg/mL MOF corresponding to 1 µM His-tag, followed by flow cytometry and confocal laser scanning microscopy (CLSM) (Figure 5, S21, S22a, S23-S26). MIL-88A and HKUST-1 MOF NPs contained huge particles with a tendency to aggregate (Figure S1, S10-S13) and showed quenching effects (Figure S18) resulting in poor detectability of cellular uptake (Figure S21). Compared to MIL-88A and HKUST-1, Zr-*fum* MOF NPs exhibit several favorable characteristics such as very narrow particle size distribution, uniform sphere morphology, low aggregation behavior, negligible fluorescence quenching and also good cellular tolerance. Thus despite their comparatively low His-tag binding capacity, they were selected to be used for further experiments. Zr-*fum*/H_6-CF showed cellular uptake in CLSM (Figure 5a, left) and flow cytometry (Figure 5a, right). Additional z-stacks of CLSM images can be found in Figures S23 and S24. The mean fluorescence intensity (MFI, inset) of cells treated with Zr-*fum*/H_6-CF increased 20-fold compared to free H_6-CF. The cellular uptake of Zr-*fum*/H_6-GFP alone is depicted in Figure S22a, S25 and S26 showing 30-fold higher MFI values compared to free H_6-GFP. A 3D reconstruction movie of a cell treated with Zr-*fum*/H_6-GFP is provided as supporting material for download.

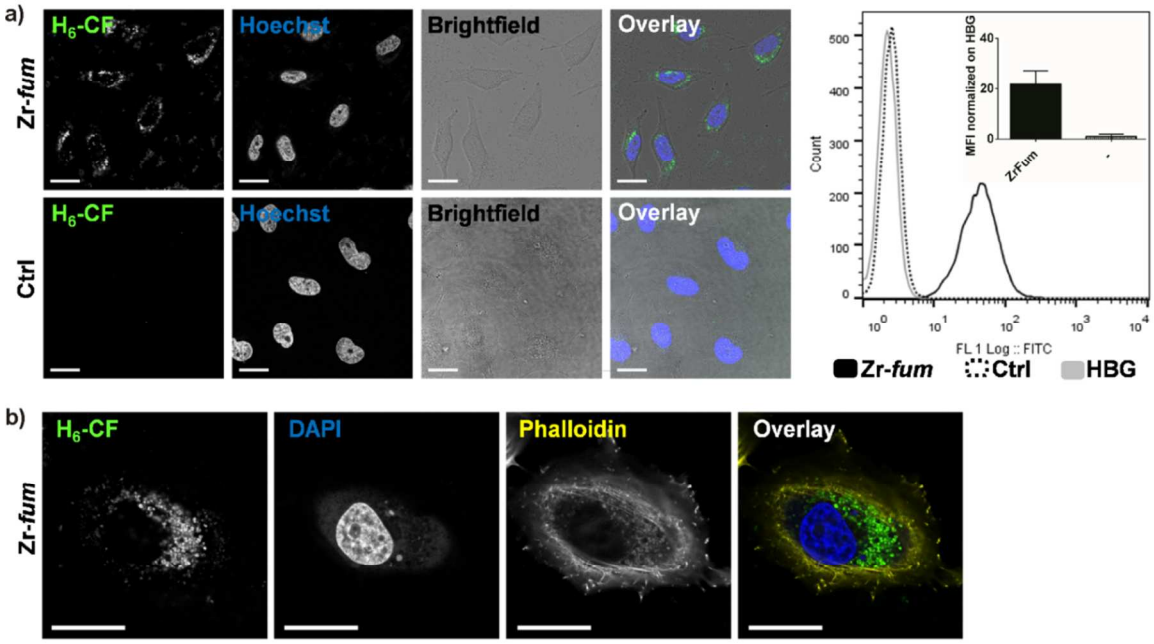

Figure 5. Cellular uptake of fluorescent peptide H_6-CF mediated by Zr-*fum* NPs. H_6-CF was incubated with Zr-*fum* MOF NPs for 15 min at room temperature in HBG for prefunctionalization by coordinative self-assembly. The functionalized particles were incubated with HeLa cells for 24 h at a concentration of 0.1 mg/mL Zr-*fum* corresponding to 1 µM H_6-CF . Solutions containing H_6-CF at same concentration but no Zr-*fum* NPs served as control (Ctrl). a) Confocal laser scanning microscopy (CLSM, left) and flow cytometry (right) after incubation of HeLa cells with functional NPs Zr-*fum*/H_6-CF (Zr-*fum*, CLSM upper row, flow cytometry solid black), H_6-CF control without Zr-*fum* NPs (Ctrl, CLSM lower row, flow cytometry dotted black) or HBG (flow cytometry grey). Mean fluorescence intensity (MFI) was normalized to HBG and is depicted in the inset. CLSM left to right: green fluorescence of H_6-CF, nuclear staining with Hoechst dye, brightfield image, overlay of all three channels. b) Enlarged CLSM image of a fixated HeLa cell after incubation with Zr-*fum*/H_6-CF. Left to right: green fluorescence of H_6-CF, nuclear staining with DAPI dye, actin staining with rhodamine-phalloidin, overlay of all three channels. Scale bar: 25 µm. Additional images can be found in the Supporting Information Figure S23 and S24.

A distinct advantage of the self-assembly concept demonstrated here is the possible one-step multifunctionalization of MOF NPs by simultaneously mixing of different H_6-tagged functional units with bare MOF NPs (Figure 1c). This procedure facilitates the creation of multifunctional MOF NPs with various stoichiometric ratios as required for optimization of spatio-temporal co-delivery into cells. As the simultaneous assembly of H_6-GFP and H_6-Tf* with Zr-*fum* MOF NPs had been confirmed by FCCS measurements (Figure 4, lower right), HeLa cells were subjected to these double-functionalized particles (Zr-*fum*/H_6-GFP+H_6-Tf*) for 24 h at a concentration of 0.1 mg/mL MOF corresponding to 0.5 µM H_6-GFP and H_6-Tf*, followed by investigation of the internalization (Figures 6, S22b). Considerable co-localization of H_6-GFP and H_6-Tf* could be observed (Figure 6a, upper row and 6b). In contrast to free H_6-GFP, free H_6-Tf* was also taken up by the cells without the addition of Zr-*fum* MOF NPs to a certain extent (Figure 6a, lower row). This can be explained by the fact that HeLa cells express the transferrin receptor (Figure S29), thus enabling receptor-mediated uptake of free H_6-Tf*. However, despite the MOF-independent uptake route of H_6-Tf*, association with Zr-*fum* resulted in 5-fold higher internalization, confirming an additional boost due to NP mediated uptake. Additional z-stacks of CLSM images can be found in Figures S27 and S28. Looking at the intracellular distribution of fluorescent peptides and proteins internalized via Zr-*fum* MOF NPs in detail, the spotty arrangement indicates high vesicular entrapment and suggests endosomal escape being a hurdle for cytosolic delivery.

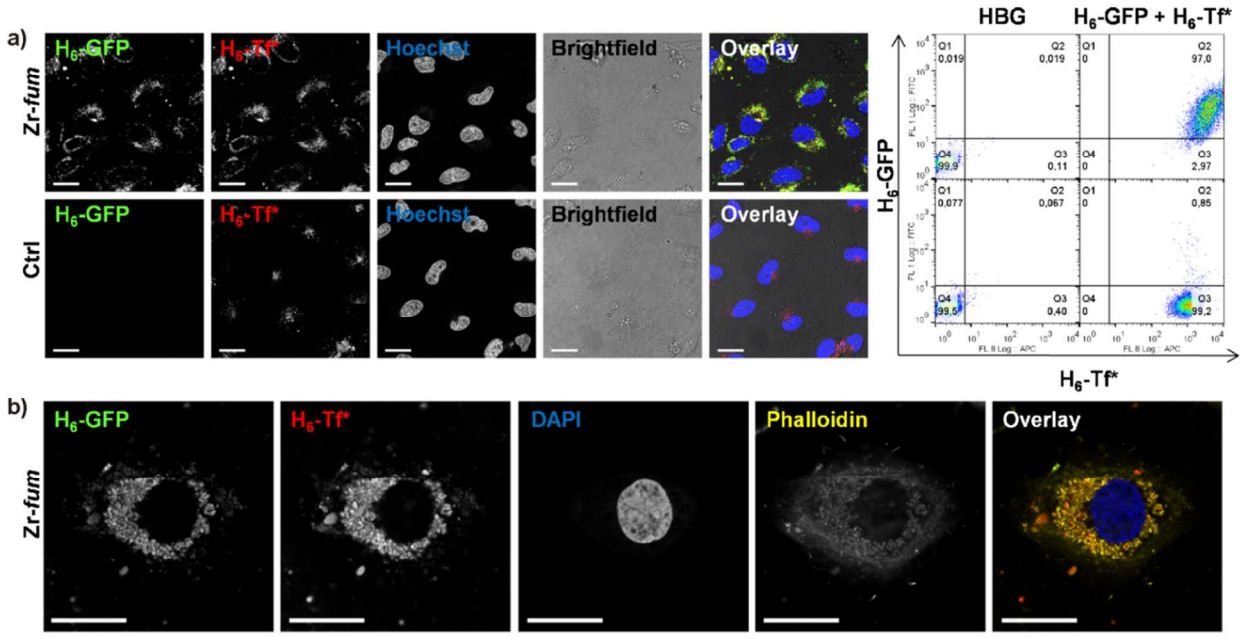

Figure 6. Simultaneous cellular uptake of fluorescent proteins H_6-GFP and H_6-Tf* mediated by Zr-*fum* NPs. An equimolar mixture of H_6-GFP and H_6-Tf* was incubated with Zr-*fum* MOF NPs for 15 min at room temperature in HBG for prefunctionalization by coordinative self-assembly. The double functionalized particles were incubated with HeLa cells for 24 h at a concentration of 0.1 mg/mL Zr-*fum* corresponding to 0.5 µM H_6-GFP and H_6-Tf*. Solutions containing H_6-GFP and H_6-Tf* at same concentration but no Zr-*fum* NPs served as control (Ctrl). a) Cellular uptake of Zr-*fum*/H_6-GFP+H_6-Tf* (upper row) or control without MOF NPs (lower row). CLSM left to right: green fluorescence of H_6-GFP, red fluorescence of H_6-Tf*, nuclear staining with Hoechst dye, brightfield picture, overlay of all four channels, yellow color indicates co-localization of H_6-GFP and H_6-Tf*. Flow cytometry analysis: HBG (left) or H_6-GFP +H_6-Tf* (right) with Zr-*fum* MOF NPs (upper row) or Ctrl without MOF NPs (lower row). b) Enlarged CLSM image of a fixated HeLa cell after incubation with Zr-*fum*/H_6-GFP+H_6-Tf*. Left to right: green fluorescence of H_6-GFP, red fluorescence of H_6-Tf*, nuclear staining with DAPI dye, actin staining with rhodamine-phalloidin, overlay of all four channels. Scale bar: 25 µm. Additional images can be found in the Supporting Information Figure S27 and S28 and a 3D reconstruction movie of a cell treated with Zr-*fum*/H_6-GFP is provided as supporting material for download.

Endocytosis mechanism. The cellular uptake pathway of Zr-*fum*/H_6-GFP NPs was investigated in an uptake experiment (Figure 7). HeLa cells were pre-incubated for 30 min at 4 °C, to reduce cellular metabolism and block energy dependent processes, or with various concentrations of the individual endocytosis inhibitors chlorpromazine (clathrin-mediated endocytosis), amiloride (macropinocytosis) and genistein (caveolae-mediated endocytosis) to discriminate the particular endocytotic routes. Afterwards the cells were subjected to Zr-*fum*/H_6-GFP NPs at a concentration of 0.1 mg/mL MOF NPs corresponding to 1 µM H_6-GFP for 2 h, followed by flow cytometric analysis in acidified PBS (pH 4, 10 % FBS) to quench the extracellular fluorescence. The results clearly show, that the NPs are internalized via an energy dependent process. Pre-incubation with amiloride showed the

greatest inhibitory effect which suggests macropinocytosis is having major contribution to the uptake of Zr-*fum*/H_6-GFP nanoparticles. Since some effect of genistein was observed, caveolae mediated uptake might also be involved to a minor extent. A recent study investigated the endocytosis mechanisms of UiO-66 (Zr^{4+}/terephthalate) MOF NPs [61]. Consistently, the cellular uptake of UiO-66 was also identified to be an energy dependent process with distinct involvement of macropinocytosis, however also major contribution of clathrin-mediated endocytosis was found.

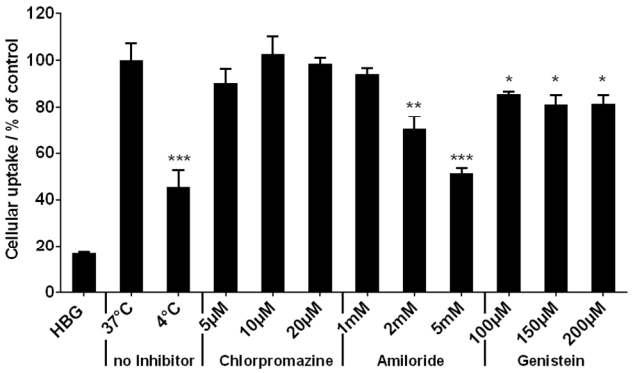

Figure 7. Evaluation of endocytosis inhibition of Zr-*fum*/H_6-GFP nanoparticles. Pre-Incubation of HeLa cells with different inhibitors or at 4 °C for 30 min, followed by incubation with Zr-*fum*/H_6-GFP for 2 h at 37 °C or 4 °C. Flow cytometric analysis was carried out in PBS (pH 4.0) to quench the extracellular fluorescence. Cellular uptake was determined as MFI. Data are presented as % cellular uptake normalized to uptake of Zr-*fum*/H_6-GFP NPs at 37 °C ± SD (*n*=3).

Transduction of biologically active peptides and proteins. To further evaluate the potential of Zr-*fum* MOF NPs as carrier system for cytosolic cargo release, transduction of membrane impermeable bioactive pro-apoptopic peptides (Bak, Bad, KLK) and mitochondrial cytochrome C (CytC) protein was investigated and cell killing was used as reporter of successful cytosolic delivery. H_6-tags were chemically conjugated to CytC or integrated at the N-terminus of the peptide sequences derived from the BH3 domain of Bak and Bad proteins[62] or the antibacterial and mitochondrial membrane-disruptive artificial peptide KLK[63,64]. Endogenous cellular CytC represents an essential part of the electron transfer chain in mitochondria but also a crucial player in the intrinsic mitochondrial apoptosis pathway after release into the cytosol[65]. Several approaches for the intracellular delivery of exogenous CytC, induction of apoptosis and cell killing have been reported before[66-69]. Notably, for the purification of H_6-CytC (and H_6-Tf*) carrying a H_6-tag after chemical conjugation, immobilized metal-ion chromatography was used, which is based on the same principle as the binding to MOFs. The utilization of the same interaction for isolation and subsequent attachment to the carrier system is considered a very convenient and robust manufacturing process. Binding of the pro-apoptotic factors to Zr-*fum* NPs was confirmed by measuring the change of zeta potential upon addition of the MOFs (Figure S30a). For biological evaluation, HeLa cells were treated with Zr-*fum*/H_6-Bak, /H_6-Bad, /H_6-KLK or /H_6-CytC (0.2 mg/mL Zr-*fum* and 10 µM peptide or protein) for 48 h. Cell viability was assessed by MTT assay and approx. 60 % cell killing could be detected in case of all functionalized Zr-*fum* NPs (Figure 8).

Without the addition of MOF NPs all pro-apoptotic factors did not exhibit any detectable toxicity up to a concentration of 20 µM (Figure S30b). These findings indicate that, despite the bottleneck of vesicular entrapment, significant fractions of cargo molecules were able to escape and induce biological effects in the cytosol.

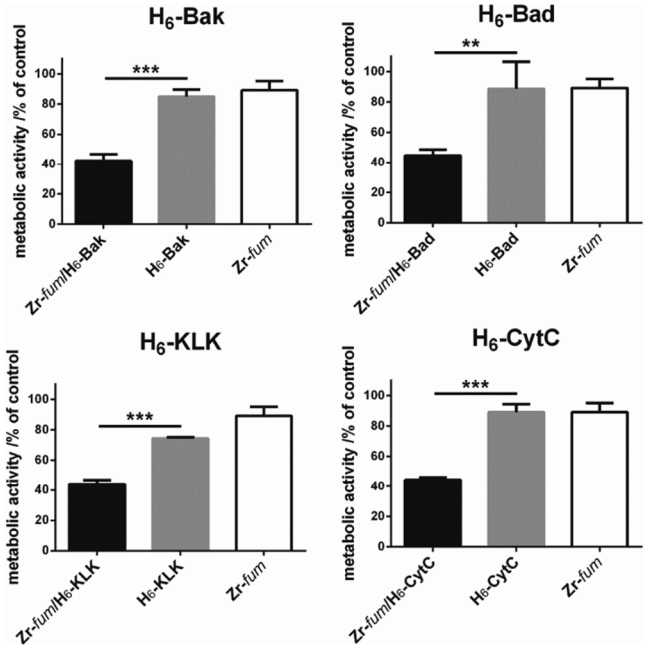

Figure 8. Intracellular transport of pro-apoptotic factors by Zr-*fum* MOF NPs and induction of HeLa cell killing upon incubation for 48 h. Final concentration of H_6-Bak, H_6-Bad, H_6-KLK, H_6-CytC was 10 µM (0.2 mg Zr-*fum*/10 nmol His-tag per mL medium). Data are presented as % metabolic activity of control cells ± SD (*n*=3) (MTT assay).

CONCLUSION

In summary, the proposed coordinative interaction of functionalized His-tags with MOF NPs was successfully established, exhibiting His-tag length and MOF species dependent binding. The fact that all investigated MOF structures showed considerable H_6-tag binding, despite their different metal components, provided flexibility for consideration of additional parameters and material characteristics (e.g. particle size distribution, aggregation behavior, fluorescence quenching and cytotoxicity) relevant for the intended purpose. The inherent properties of the individual compounds (His-tag containing functional units, MOF NPs) and the reversible nature of interaction account for the strength of the approach. Numerous available recombinant proteins already contain His-tags or they can readily be integrated in peptidic structures by conjugation. For biomedical applications, MOF NPs are promising materials due to their precise assembly of an

enormous number of inorganic and organic molecular building blocks resulting in a highly variable chemical composition, porosity and degradability into their small building units. The MOF structural designability at the molecular level chemistry together with an extension of the functional unit library opens the perspective to generate a variety of "self-assembling multifunctional coordination particles" (SAMCOPs) by simple combinatorial and stoichiometric mixing. In this respect, this work presents a versatile functionalization concept of MOF NPs with great potential for co-delivery of proteins, drugs or other pharmacologically active agents, including those that can be adsorbed within the pore systems.

METHODS

Synthesis of MIL-88A.MIL-88A were synthesized using an approach based on the results of Chalati *et al.*[52] FeCl3 x 6 H2O (1.084 g, 4.01 mmol) and fumaric acid (485 mg, 4.18 mmol) were given into water (20 mL). After $FeCl_3$ x $6H_2O$ was completely dissolved, the reaction vessel was placed in a microwave reactor (Synthos 3000, Anton Paar). In addition to the reaction vessel, a reference vessel containing an aqueous solution of $FeCl_3$ x $6H_2O$ (1.080 g, 20 mL) and 2 vessels containing water (20 mL) were placed in the microwave reactor. The sample was heated in 30 sec to 80 °C, stayed at 80 °C for 5 min and cooled down to room temperature in 1 h.

Synthesis of HKUST-1. The synthesis of HKUST-1 was conducted following a method shown by Huo *et al.*[47] $Cu(NO_3)_2$ x $2.5H_2O$ (70 mg, 0.30 mmol) was dissolved in water (6 mL). Trimesic acid (126 mg, 0.60 mmol) was added to this solution under stirring. The reaction mixture was left stirring for 60 min. Subsequently, the resulting product was washed via centrifugation (15 min, 8750 rpm). The supernatant was removed and the precipitated nanoparticles were dispersed in ethanol (6 mL). This washing cycle was repeated three times to yield the final product.

Synthesis of Zr-*fum*. Zr-*fum* were synthesized using an approach based on the results of Wißmann et al.[48] $ZrCl_4$ (120.4 mg, 0.52 mmol) and fumaric acid (180.1 mg, 1.54 mmol) were given into a glass vessel (25 mL). A mixture of water (10 mL) and formic acid (975 µL) was added to the glass reactor. After sealing the reactor the dispersion was placed in an oven (120 °C) for 24 h. Subsequently, the reaction mixture was cooled down to room temperature followed by separation into 8 equal portions. The nanoparticle dispersions were washed in a first step via centrifuging (4 min, 14000 rpm) and subsequent redispersion in water (8 x 1.5 mL) under sonication. The samples were further washed in three additional washing cycles comprising centrifugation (4 min, 14000 rpm), removal of the supernatant, and redispersion of the remaining nanoparticles in ethanol (8 x 1.5 mL). Afterwards, the 8 dispersions were reunified.

Preparation of MOF suspension in HBG. MOF suspensions in HBG were always freshly prepared prior to performing the experiment. The necessary amount of MOF material in ethanol was centrifuged (10 min, 10000 rpm), and the supernatant was removed. The MOF pellet was resuspended in HBG (pH 7.4) at a final concentration of 5 or 10 mg/mL by continuous pipetting, followed by 10 min sonication.

Investigation of peptide binding (A_6, H_6) by RP-HPLC. 3 µL of a solution containing equimolar amounts of H_6-Acr and A_6-Acr (5 mM) in HBG (pH 7.4) were added to 47 µL HBG in a 1.5 mL reaction tube. 100 µL of MOF suspension (5 mg/mL in HBG, pH 7.4) were added and vortexed briefly. As control, 100 µL HBG without MOF particles were added to an analogous sample. The mixtures were incubated at room temperature for 15 min under shaking and centrifuged for 10 min at 13400 rpm. Subsequently, 120 µL of the supernatant were transferred into HPLC sample vials. RP-HPLC analysis was carried out using a YMC Pack Pro C18 RS column (250 x 4.6 mm) connected to a VWR Hitachi Chromaster HPLC system (5160 pump module, 5260 auto sampler, 5310 column oven, 5430 diode array detector). 10 µL of the samples were injected and a gradient from 5 % acetonitrile (0.1 % TFA) to 100 % acetonitrile (0.1 % TFA) over 15 min was used for the analysis. Acridine containing compounds were detected photometrically at 360 nm.

Zeta potential measurements of MOF nanoparticle functionalization. 3 nmol H_6-Acr or A_6-Acr were diluted in HBG (pH 7.4) buffer. In case of pro-apoptotic peptides and CytC 5 nmol were used. 100 µg MOF NPs (5 mg/mL, HBG pH 7.4) were added (final volume 30 µL) and samples were incubated at room temperature for 15 min with shaking. Shortly before the measurement in a folded capillary cell (DTS1070), samples were diluted to a final MOF concentration of 0.1 mg/mL. Zeta potential was measured by electrophoretic laser-light scattering using a Zetasizer Nano ZS (Malvern Instruments, Worcestershire, U.K.). Zeta potentials were calculated by the Smoluchowski equation, each sample was measured 3 times with 10 to 30 subruns at 25 °C.

Quantitative determination of H_0-, H_3-, H_6-Acr binding to MOF NPs. A solution containing a total amount of 130 nmol oligopeptide-based structure to be examined was prepared in HBG. The required amount of 10 mg/mL MOF nanoparticles dispersed in HBG was added featuring a total volume of 1 mL. Right after the addition of the MOF nanoparticles, samples were briefly vortexed. After subsequent incubation (15 min, 25 °C, 600 rpm) and centrifugation (5 min, 14000 rpm) 100 µL of supernatant were collected and photometrically measured at 360 nm against HBG as a blank. For each examined oligopeptide-based structure, a control of 130 nmol peptide without MOF in a total volume of 1 mL was also prepared and measured (n=3). To obtain the amount of bound peptide, the absorption of the supernatant - representing the amount of peptide that remained in solution and thereby unbound by the MOF - was subtracted from the average absorption of the MOF free control: A(bound) = A(control) – A(supernatant). Final binding values were calculated as follows, % (bound) = A(bound)/A(control) x 100. The average of % bound determined by three independent measurements ±SD was plotted.

Investigation of binding stability of H_6-tags to Zr-*fum* and pH dependent release. In order to evaluate

the stable binding and extent of acidic release of His-tags and Zr-*fum* MOF NPs over a longer period, Zr-*fum* NPs in HBG were loaded with H_6-A647N. 50 µL of the freshly prepared Zr-*fum* NPs were diluted in ~500 µL HBG pH 7.4 (depending on the amount of HCl added to the sample in the next step), followed by addition of 4 µL 1 mM H_6-A647N. The HBG volume therefore slightly varied in order to always allow for equal final sample volumes of 500 µL. Samples were briefly vortexed and incubated under agitation for 15 min (25 °C, 600 rpm, light protection). Afterwards, samples were acidified to pH 3, pH 5 and pH 7.4 by addition of 9.2 µL, 4.5 µL or 0 µL 1 M HCl respectively. After 0.5 h, 3 h and 24 h, the respective samples were centrifuged (5 min, 14000 rpm). The presence of free dye in the supernatant was determined photometrically at 646 nm (n=3). Independent samples were used for each time point.

Fluorescence Correlation Spectroscopy (FCS). The non-fluorescent MOF nanoparticles are not detectable by the FCS unless fluorescently labeled His-tags are attached to the NPs. Thus a shift to higher diffusion times of the correlation curve after addition of NPs to fluorescently labeled His-tags certifies the binding of His-tags to the NPs surface. Normalization of autocorrelation curves helps to clearly visualize that the autocorrelation function of the MOF/His-tag is shifted towards higher correlation times with respect to the free His-tag molecules. Dual-color fluorescence Cross-Correlation Spectroscopy (FCCS) allows for a comparison between spectrally separated channels to extract codiffusion events that reflect interactions between differently labeled molecules.[70,71] For FCS and FCCS measurements, an Axiovert 200 microscope with a ConfoCor 2unit (Carl Zeiss, Jena, Germany) equipped with a 40x (NA 1.2) water immersion apochromat objective (Carl Zeiss) was used. A helium neon laser (633 nm) and for FCCS additionally an argon laser (488 nm) was used for illumination. Samples were measured in eight-well LabTekchamber slides (Nunc, Rochester, NY). If nothing else mentioned, measurements were performed in HBG pH 7.4 at a temperature of 22.5 °C. Correlation was performed using ConfoCor 2 software. A detailed description of the various experimental setups of FCS and FCCS measurements and the theory of FCS can be found in the Supporting Information.

Cell culture. HeLa cells were grown in Dulbecco's Modified Eagle's Medium (DMEM) (1000 mg/mL glucose, L-glutamine and sodium bicarbonate) supplemented with 10 % FBS, 100 U/mL penicillin, 100 µg/mL streptomycin at 37 °C and 5 % CO_2 in a humidified incubator.

Cellular uptake experiments using flow cytometric analysis. Cells were seeded in 24-well plates (Corning Costar, Sigma-Aldrich, Germany) at a density of 20.000 cells/well. After 24 h, medium was replaced with 400 µL fresh medium. 0.5 nmol H_6-CF or H_6-GFP were diluted in HBG (pH 7.4), 50 µg MOF NPs (5 mg/mL in HBG, pH 7.4) were added (final volume 50 µL) and the solution was strongly mixed. For the co-delivery of H_6-GFP and H_6-Tf*, 0.25 nmol H_6-GFP and 0.25 nmol H_6-Tf* were pre-mixed in HBG (pH 7.4) before 50 µg Zr-*fum* MOF NPs (5 mg/mL in HBG, pH 7.4) were added (final volume 50 µL). The mixtures were incubated for 15 min at room temperature, diluted 1:2 with HBG (pH 7.4, final volume 100 µL) and added to the cells (100 µL MOF/His-tag solution per well). Controls were performed without the addition of MOF NPs. Cells were incubated for 24 h at 37 °C and 5 % CO_2 in a humidified incubator. In case of HKUST-1 MOF NPs, medium was changed after 2 h and cells were incubated for further 22 h in fresh medium. Cells were washed with PBS (pH 7.4), detached with trypsin/ EDTA and diluted with fresh medium. Cells were centrifuged and resuspended in 500 µL PBS containing 10 % FBS at pH 4 to quench extracellular fluorescence. 500 ng/µL DAPI (4',6-diamidino-2-phenylindole) were added shortly before the measurement. The cellular fluorescence was assayed by excitation of DAPI at 405 nm and detection of emission at 450 nm, fluorescein at 488 nm and detection of emission at 510 nm. For the co-delivery of H_6-GFP and H_6-Tf* the cellular fluorescence was also assayed by excitation of A647N at 635 nm and detection of emission at 665 nm. Cells were appropriately gated by forward/ sideward scatter and pulse width for exclusion of doublets. DAPI was used to discriminate between viable and dead cells. Data were recorded by Cyan™ ADP flow cytometer (Dako, Hamburg, Germany) using Summit™ acquisition software (Summit, Jamesville, NY). Ten thousand gated cells per sample were collected. Analysis was done by FlowJo 7.6.5 flow cytometric analysis software. All experiments were performed in triplicates. MFI was calculated by FlowJo 7.6.5 flow cytometric analysis software and is depicted as normalization to HBG ± SD (n=3).

Confocal laser scanning microscopy. Cells were seeded in 8-Well Nunc chamber slights (Thermo Scientific, Germany) at a density of 12.000 cells/well. Wells were coated with collagen A prior to seeding. After 24 h medium was replaced with 240 µL fresh medium. The various samples were prepared in the same way as has been described above but in a final volume of 60 µL HBG. 30 µg MOF NPs were functionalized with 0.3 nmol H_6-CF or H_6-GFP in 30 µL HBG (pH 7.4). In case of the co-delivery experiment, 0.15 nmol H_6-GFP were mixed with 0.15 nmol H_6-Tf* before the addition of 30 µg Zr-fum MOF NPs. After incubation of the mixtures for 15 min at room temperature, they were diluted 1:2 in HBG (pH 7.4, final volume 60 µL). The mixtures were added to the cells (60 µL MOF/His-tag solution per well) and incubated for 24 h. Controls were performed without the addition of MOF NPs. In case of HKUST-1 MOF NPs, the medium was changed after 2 h and cells were incubated for further 22 h in fresh medium. Prior to imaging nuclei were stained with Hoechst dye (500 ng/µL). Medium was replaced by DMEM without phenol red supplemented with 10 % FBS, 100 U/mL penicillin, 100 µg/mL streptomycin and cells were imaged using a Leica TCS SP8 confocal microscope with an 63x DIC oil immersion objective (Plan-APOCHROMAT). For imaging of z-stacks, cells were fixated for 30 min, using 4 % (w/v) paraformaldehyde solution followed by 3 washes with PBS (pH 7.4). The nucleus was stained with DAPI (500 ng/µL), and Actin with rhoadmine-phalloidin (2 µL/mL) for 15 min at room temperature. Staining solution was replaced with

PBS (pH 7.4) and cells were stored at 4 °C. Images were recorded with a z-distance of 0.3 µm from basolateral (top) to apical (bottom) pole of a representative cell. Pictures were taken at 405 nm (Hoechst dye or DAPI), 488 nm (H_6-GFP or H_6-CF), 514 nm (rhodamine-phalloidine), 633 nm (Atto647N).

Endocytosis inhibitory assay. HeLa cells were seeded in 24-Well plates (Corning Costar, Sigma-Aldrich, Germany) at a density of 50.000 cells/well. After 24 h, medium was replaced with 400 µL fresh medium containing the different endocytosis inhibitors, chlorpromazine (final concentration 5 µM, 10 µM, 20 µM), amiloride (final concentration 1 mM, 2 mM, 5 mM) and genistein (final concentration 100 µM, 150 µM, 200 µM). Cells were pre-incubated with the different inhibitors or at 4 °C for 30 min before addition of the H_6-GFP/Zr-*fum* MOF NPs. 0.5 nmol H_6-GFP were diluted in HBG (pH 7.4), 50 µg Zr-*fum* MOF NPs (5 mg/mL in HBG, pH 7.4) were added (final volume 50 µL) and the solution was strongly mixed. The mixture was incubated for 15 min at room temperature, diluted 1:2 with HBG (pH 7.4, final volume 100 µL) and added to the cells (100 µL Zr-*fum*/H_6-GFP solution per well). Cells were incubated for 2 h at 37 °C and 5 % CO_2 or at 4 °C. Cells were washed with PBS (pH 7.4), detached with trypsin/EDTA and diluted with fresh medium. Cells were centrifuged and resuspended in 500 µL PBS containing 10 % FBS at pH 4 to quench extracellular fluorescence. 500 ng/µL DAPI (4',6-diamidino-2-phenylindole) were added shortly before the measurement. The cellular fluorescence was assayed by excitation of DAPI at 405 nm and detection of emission at 450 nm and fluorescein at 488 nm and detection of emission at 510 nm. Cells were appropriately gated by forward/ sideward scatter and pulse width for exclusion of doublets. DAPI was used to discriminate between viable and dead cells. Data were recorded by Cyan™ ADP flow cytometer (Dako, Hamburg, Germany) using Summit™ acquisition software (Summit, Jamesville, NY). Five thousand gated cells per sample were collected. Analysis was done by FlowJo 7.6.5 flow cytometric analysis software. Data is presented as % cellular uptake, of cellular uptake of Zr-*fum*/H_6-GFP NPs at 37 °C ±SD (n=3).

Delivery of pro-apoptopic peptides and CytC. Cells were seeded in 96-Well plates (Corning Costar, Sigma-Aldrich, Germany) at a density of 4.000 cells/well. After 24 h, medium was replaced with 80 µL fresh medium. 1 nmol of H_6-Bak, H_6-Bad, H_6-KLK or H_6-CytC was diluted in HBG (pH 7.4), 20 µg Zr-*fum* MOF NPs (5 mg/mL in HBG pH 7.4) were added followed by strongly mixing of the samples (final volume 10 µL). Controls were performed without the addition of Zr-f*um* MOF NPs. The mixtures were incubate for 15 min at room temperature, diluted 1:2 with HBG (pH 7.4, final volume 20 µL), added to the cells (20 µL Zr-*fum*/His-tag solution per well) and incubated for 48 h. Analysis of cytotoxicity was carried out by MTT assay, as is described in the following.

Cell viability assay. Cells were seeded in 96-well plates (Corning Costar, Sigma-Aldrich, Germany) at a density of 4000 cells/well. After 24 h medium was replaced with 80 µL fresh medium. The appropriate amount of compound to be tested was diluted in HBG (pH 7.4) and 20 µL of each sample/well were added. Cells were incubated for 48 h at 37 °C and 5 % CO_2 in a humified incubator. 10 µL of MTT (3-(4,5-dimethylthia-zol-2-yl)-2,5-diphenyltetrazolium bromide) (5 mg/mL) were added to each well reaching a final concentration of 0.5 mg/mL. After an incubation time of 2 h, unreacted dye and medium were removed and the 96-well plates were frozen at –80 °C for at least 30 min. To dissolve the purple formazan product 100 µL DMSO were added per well and the plate was incubated for 30 min at 37 °C with shaking. The wells were quantified by measuring absorbance at 590 nm with background correction at 630 nm using a microplate reader (TecanSpectrafluor Plus, Tecan, Switzerland). All studies were performed in triplicates. The relative cell viability (%) related to control wells treated only with 20 µL HBG (pH 7.4) was calculated as ([A] test/[A] control) × 100 %.

Statistical analysis. The statistical significance of experiments were analyzed using the t-test, **** p≤0.0001, *** p≤0.001, ** p≤0.01, * p≤0.05.

ASSOCIATED CONTENT

Supporting Information. Additional Materials and Methods, synthesis and analysis of peptides and His-tagged functional units, characterization of MOF NPs, Supplementary Figures. This material is available free of charge via the Internet at http://pubs.acs.org.

AUTHOR INFORMATION

Corresponding Author

*ulrich.laechelt@cup.uni-muenchen.de,
stefan.wuttke@cup.lmu.de

Author Contributions

The manuscript was written through contributions of all authors. All authors have given approval to the final version of the manuscript.

ACKNOWLEDGMENT

We are grateful for financial support from the Excellence Cluster Nanosystems Initiative Munich (NIM) and the Center for NanoScience Munich (CeNS). Funding through the DFG SFB 1032 and DFG project WU 622/4-1 is greatly appreciated. We thank Olga Brück and Wofgang Rödl for technical assistance and appreciate the help of cameraman Michael Beetz.

ABBREVIATIONS

A647N, ATTO647N; Acr, acridine; CF, carboxyfluorescein; CLSM, confocal laser scanning microscopy; CUS, coordinatively unsaturated metal sites; CytC, cytochrome C; DLS, dynamic light scattering; FCS, fluorescence correlation spectroscopy; FCCS, fluorescence cross-correlation spectroscopy; GFP, green fluorescent protein; HBG, HEPES buffered glucose; MFI, mean fluorescence intensity; MOF, metal-organic framework; NP, nanoparticle; SEM, scanning electron microscopy; SAMCOPs, self-assembling multifunctional nanoparticles; TGA, thermogravimetric analysis; Tf, transferrin; XRD, X-ray diffraction

REFERENCES

(1) Goesmann, H.; Feldmann, C. *Angew Chem Int Ed Engl* **2010**, *49*, 1362.

(2) Tibbitt, M. W.; Dahlman, J. E.; Langer, R. *J Am Chem Soc* **2016**, *138*, 704.

(3) Calandra, P.; Caschera, D.; Turco Liveri, V.; Lombardo, D. *Colloids and Surfaces A: Physicochemical and Engineering Aspects* **2015**, *484*, 164.

(4) Torchilin, V. P. *Pharm Res* **2007**, *24*, 1.

(5) Nishiyama, N.; Matsumura, Y.; Kataoka, K. *Cancer Sci* **2016**, *107*, 867.

(6) Discher, B. M.; Won, Y. Y.; Ege, D. S.; Lee, J. C.; Bates, F. S.; Discher, D. E.; Hammer, D. A. *Science* **1999**, *284*, 1143.

(7) Davis, M. E. *Mol Pharm* **2009**, *6*, 659.

(8) Park, I. K.; von Recum, H. A.; Jiang, S.; Pun, S. H. *Langmuir* **2006**, *22*, 8478.

(9) Sanvicens, N.; Marco, M. P. *Trends Biotechnol* **2008**, *26*, 425.

(10) Jia, F.; Liu, X.; Li, L.; Mallapragada, S.; Narasimhan, B.; Wang, Q. *J Control Release* **2013**, *172*, 1020.

(11) Torchilin, V. P. *Annu.Rev.Biomed Eng* **2006**, *8*, 343.

(12) Fu, A.; Tang, R.; Hardie, J.; Farkas, M. E.; Rotello, V. M. *Bioconjug Chem* **2014**, *25*, 1602.

(13) Furukawa, H.; Cordova, K. E.; O'Keeffe, M.; Yaghi, O. M. *Science* **2013**, *341*, 1230444.

(14) Zhou, H. C.; Long, J. R.; Yaghi, O. M. *Chem Rev* **2012**, *112*, 673.

(15) Zhou, H. C.; Kitagawa, S. *Chem Soc Rev* **2014**, *43*, 5415.

(16) Horcajada, P.; Chalati, T.; Serre, C.; Gillet, B.; Sebrie, C.; Baati, T.; Eubank, J. F.; Heurtaux, D.; Clayette, P.; Kreuz, C.; Chang, J. S.; Hwang, Y. K.; Marsaud, V.; Bories, P. N.; Cynober, L.; Gil, S.; Ferey, G.; Couvreur, P.; Gref, R. *Nat Mater* **2010**, *9*, 172.

(17) Baati, T.; Horcajada, P.; Gref, R.; Couvreur, P.; Serre, C. *J Pharm Biomed Anal* **2011**, *56*, 758.

(18) Wuttke, S.; Zimpel, A.; Bein, T.; Braig, S.; Stoiber, K.; Vollmar, A.; Muller, D.; Haastert-Talini, K.; Schaeske, J.; Stiesch, M.; Zahn, G.; Mohmeyer, A.; Behrens, P.; Eickelberg, O.; Bolukbas, D. A.; Meiners, S. *Adv Healthc Mater* **2016**, DOI: 10.1002/adhm.201600818 [Epub ahead of print].

(19) Taylor-Pashow, K. M.; Della Rocca, J.; Xie, Z.; Tran, S.; Lin, W. *J Am Chem Soc* **2009**, *131*, 14261.

(20) Zheng, H.; Zhang, Y.; Liu, L.; Wan, W.; Guo, P.; Nystrom, A. M.; Zou, X. *J Am Chem Soc* **2016**, *138*, 962.

(21) Yang, Y.; Hu, Q.; Zhang, Q.; Jiang, K.; Lin, W.; Yang, Y.; Cui, Y.; Qian, G. *Mol Pharm* **2016**, *13*, 2782.

(22) Wuttke, S.; Braig, S.; Preiss, T.; Zimpel, A.; Sicklinger, J.; Bellomo, C.; Radler, J. O.; Vollmar, A. M.; Bein, T. *Chem Commun (Camb)* **2015**, *51*, 15752.

(23) He, C.; Lu, K.; Liu, D.; Lin, W. *J Am Chem Soc* **2014**, *136*, 5181.

(24) Tan, L.-L.; Li, H.; Qiu, Y.-C.; Chen, D.-X.; Wang, X.; Pan, R.-Y.; Wang, Y.; Zhang, S. X.-A.; Wang, B.; Yang, Y.-W. *Chem Sci* **2015**, *6*, 1640.

(25) Wang, X. G.; Dong, Z. Y.; Cheng, H.; Wan, S. S.; Chen, W. H.; Zou, M. Z.; Huo, J. W.; Deng, H. X.; Zhang, X. Z. *Nanoscale* **2015**, *7*, 16061.

(26) Levine, D. J.; Runcevski, T.; Kapelewski, M. T.; Keitz, B. K.; Oktawiec, J.; Reed, D. A.; Mason, J. A.; Jiang, H. Z.; Colwell, K. A.; Legendre, C. M.; FitzGerald, S. A.; Long, J. R. *J Am Chem Soc* **2016**, *138*, 10143.

(27) Zhuang, J.; Kuo, C. H.; Chou, L. Y.; Liu, D. Y.; Weerapana, E.; Tsung, C. K. *ACS nano* **2014**, *8*, 2812.

(28) Wuttke, S.; Lismont, M.; Escudero, A.; Rungtaweevoranit, B.; Parak, W. J. *Biomaterials* **2017**, *accepted*.

(29) Liang, K.; Ricco, R.; Doherty, C. M.; Styles, M. J.; Bell, S.; Kirby, N.; Mudie, S.; Haylock, D.; Hill, A. J.; Doonan, C. J.; Falcaro, P. *Nature communications* **2015**, *6*, 7240.

(30) Liang, K.; Coghlan, C. J.; Bell, S. G.; Doonan, C.; Falcaro, P. *Chem Commun (Camb)* **2016**, *52*, 473.

(31) Lu, K.; He, C.; Lin, W. *J Am Chem Soc* **2015**, *137*, 7600.

(32) Park, J.; Feng, D.; Yuan, S.; Zhou, H. C. *Angew Chem Int Ed Engl* **2015**, *54*, 430.

(33) Liu, J.; Yang, Y.; Zhu, W.; Yi, X.; Dong, Z.; Xu, X.; Chen, M.; Yang, K.; Lu, G.; Jiang, L.; Liu, Z. *Biomaterials* **2016**, *97*, 1.

(34) Lismont, M.; Dreesen, L.; Wuttke, S. *Adv Funct Mater* **2017**, *accepted*.

(35) Horcajada, P.; Gref, R.; Baati, T.; Allan, P. K.; Maurin, G.; Couvreur, P.; Ferey, G.; Morris, R. E.; Serre, C. *Chem Rev* **2012**, *112*, 1232.

(36) Rungtaweevoranit, B.; Zhao, Y.; Min Choi, K.; Yaghi, O. M. *Nano Research* **2016**, *9*, 47.

(37) Furukawa, S.; Reboul, J.; Diring, S.; Sumida, K.; Kitagawa, S. *Chem Soc Rev* **2014**, *43*, 5700.

(38) He, C.; Liu, D.; Lin, W. *Chem Rev* **2015**, *115*, 11079.

(39) Zimpel, A.; Preiß, T.; Röder, R.; Engelke, H.; Ingrisch, M.; Peller, M.; Rädler, J. O.; Wagner, E.; Bein, T.; Lächelt, U.; Wuttke, S. *Chemistry of Materials* **2016**, *28*, 3318.

(40) McGuire, C. V.; Forgan, R. S. *Chemical Communications* **2015**, *51*, 5199.

(41) Block, H.; Maertens, B.; Spriestersbach, A.; Brinker, N.; Kubicek, J.; Fabis, R.; Labahn, J.; Schafer, F. *Methods Enzymol* **2009**, *463*, 439.

(42) Hochuli, E.; Bannwarth, W.; Döbeli, H.; Gentz, R.; D, S. *Nat Biotechnol* **1988**, *6*, 1321

(43) June, R. K.; Gogoi, K.; Eguchi, A.; Cui, X. S.; Dowdy, S. F. *J Am Chem Soc* **2010**, *132*, 10680.

(44) Wieneke, R.; Laboria, N.; Rajan, M.; Kollmannsperger, A.; Natale, F.; Cardoso, M. C.; Tampe, R. *J Am Chem Soc* **2014**, *136*, 13975.

(45) Postupalenko, V.; Desplancq, D.; Orlov, I.; Arntz, Y.; Spehner, D.; Mely, Y.; Klaholz, B. P.; Schultz, P.; Weiss, E.; Zuber, G. *Angew Chem Int Ed Engl* **2015**, *54*, 10583.

(46) Chiu, H. Y.; Deng, W.; Engelke, H.; Helma, J.; Leonhardt, H.; Bein, T. *Sci Rep* **2016**, *6*, 25019.

(47) Huo, J.; Brightwell, M.; El Hankari, S.; Garai, A.; Bradshaw, D. *J Mater Chem* **2013**, *1*, 15220.

(48) Wißmann, G.; Schaate, A.; Lilienthal, S.; Bremer, I.; Schneider, A. M.; Behrens, P. *Microporous Mesoporous Mater* **2012**, *152*, 64.

(49) Zahn, G.; Schulze, H. A.; Lippke, J.; König, S.; Sazama, U.; Fröba, M.; Behrens, P. *Microporous Mesoporous Mater* **2015**, *203*, 186.

(50) Ueda, E. K.; Gout, P. W.; Morganti, L. *Journal of chromatography. A* **2003**, *988*, 1.

(51) Gaberc-Porekar, V.; Menart, V. *Journal of biochemical and biophysical methods* **2001**, *49*, 335.

(52) Chalati, T.; Horcajada, P.; Gref, R.; Couvreur, P.; Serre, C. *J Mater Chem* **2011**, *21*, 2220.

(53) Baati, T.; Njim, L.; Neffati, F.; Kerkeni, A.; Bouttemi, M.; Gref, R.; Najjar, M.; Zakhama, A.; Couvreur, P.; Serre, C.; Horcajada, P. *Chem Sci* **2013**, *4*, 1597.

(54) Li, K.-Y. A.; Chang, H.-A.; Hsu, C.-J. *RCS Advances* **2015**, *5*, 32520.

(55) McKinlay, A. C.; Eubank, J. F.; Wuttke, S.; Xiao, B.; Wheatley, P. S.; Bazin, P.; Lavalley, J.-C.; Daturi, M.; Vimont, A.; De Weireld, G.; Horcajada, P.; Serre, C.; Morris, R. E. *Chemistry of Materials* **2013**, *25*, 1592.

(56) Hirschle, P.; Prei; Auras, F.; Pick, A.; Volkner, J.; Valdeperez, D.; Witte, G.; Parak, W. J.; Radler, J. O.; Wuttke, S. *CrystEngComm* **2016**, *18*, 4359.

(57) Tay, C. Y.; Setyawati, M. I.; Xie, J.; Parak, W. J.; Leong, D. T. *Adv Funct Mater* **2014**, *24*, 5936.
(58) Martin, R.; Edsall, J. *J Am Chem Soc* **1960**, *82*, 1107.
(59) Dietl, C.; Hintz, H.; Ruhle, B.; Schmedt Auf der Gunne, J.; Langhals, H.; Wuttke, S. *Chemistry* **2015**, *21*, 10714.
(60) Wuttke, S.; Dietl, C.; Hinterholzinger, F. M.; Hintz, H.; Langhals, H.; Bein, T. *Chem Commun (Camb)* **2014**, *50*, 3599.
(61) Orellana-Tavra, C.; Mercado, S. A.; Fairen-Jimenez, D. *Adv Healthc Mater* **2016**, *5*, 2261.
(62) Li, R.; Boehm, A. L.; Miranda, M. B.; Shangary, S.; Grandis, J. R.; Johnson, D. E. *Neoplasia* **2007**, *9*, 801.
(63) Javadpour, M. M.; Juban, M. M.; Lo, W. C.; Bishop, S. M.; Alberty, J. B.; Cowell, S. M.; Becker, C. L.; McLaughlin, M. L. *J Med Chem* **1996**, *39*, 3107.
(64) Ellerby, H. M.; Arap, W.; Ellerby, L. M.; Kain, R.; Andrusiak, R.; Rio, G. D.; Krajewski, S.; Lombardo, C. R.; Rao, R.; Ruoslahti, E.; Bredesen, D. E.; Pasqualini, R. *Nat Med* **1999**, *5*, 1032.
(65) Bratton, S. B.; Salvesen, G. S. *J Cell Sci* **2010**, *123*, 3209.
(66) Kim, S. K.; Foote, M. B.; Huang, L. *Biomaterials* **2012**, *33*, 3959.
(67) Zhang, J.; Wu, L.; Meng, F.; Wang, Z.; Deng, C.; Liu, H.; Zhong, Z. *Langmuir* **2012**, *28*, 2056.
(68) Ng, D. Y.; Fahrer, J.; Wu, Y.; Eisele, K.; Kuan, S. L.; Barth, H.; Weil, T. *Adv Healthc Mater* **2013**, *2*, 1620.
(69) Mendez, J.; Morales Cruz, M.; Delgado, Y.; Figueroa, C. M.; Orellano, E. A.; Morales, M.; Monteagudo, A.; Griebenow, K. *Mol Pharm* **2014**, *11*, 102.
(70) Schwille, P.; Meyer-Almes, F. J.; Rigler, R. *Biophys J* **1997**, *72*, 1878.
(71) Rigler, R.; Földes-Papp, Z.; Meyer-Almes, F. J.; C., S.; M., V.; A., S. *J Biotechnol* **1998**, *63*, 97.

Insert Table of Contents artwork here

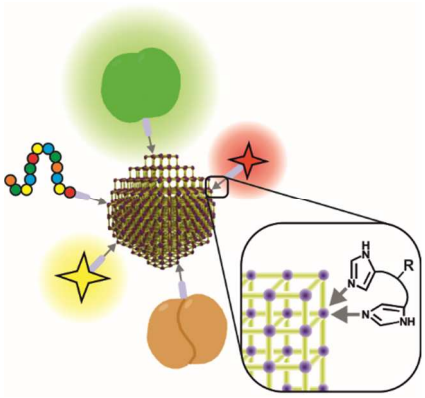

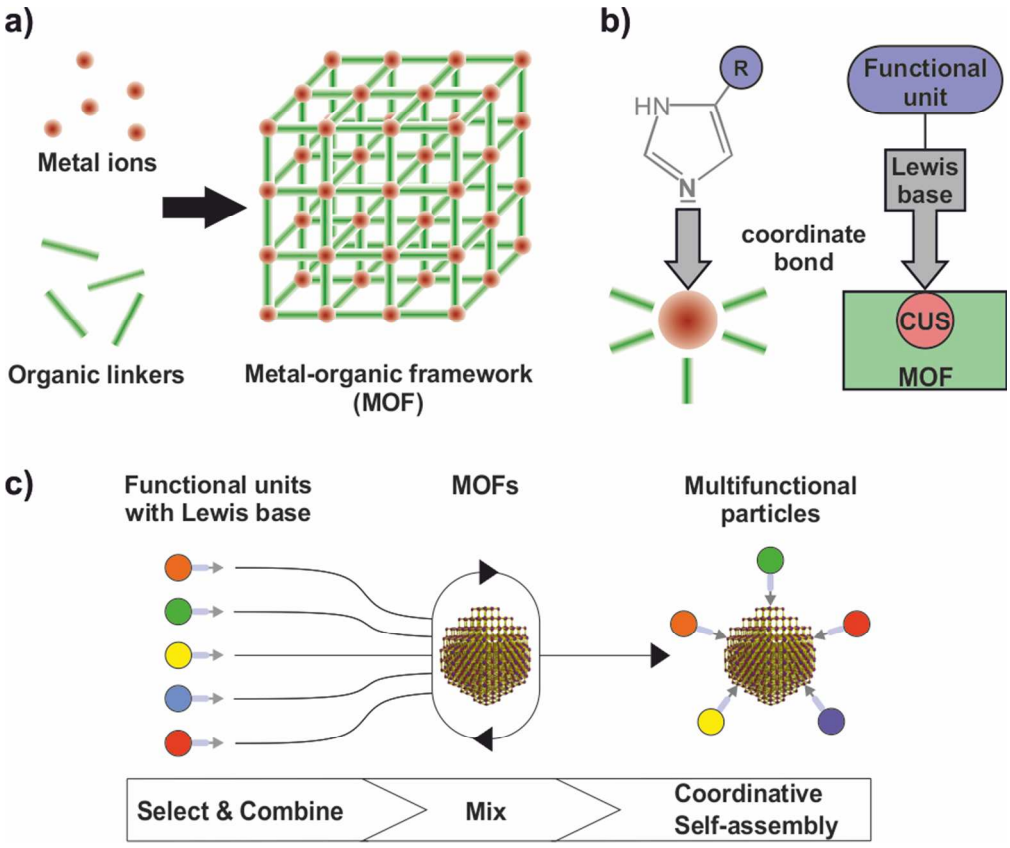

Figure 1. Illustration of coordinative self-assembly of His-tagged molecules with MOF NPs: a) molecular composition of MOFs; b) coordinative bond between the imidazole group of histidines acting as Lewis base and coordinatively unsaturated metal sites (CUS) acting as Lewis acid; c) multi-functional MOF NPs generated by coordinative attachment of different functional units via self-assembly.

86x71mm (300 x 300 DPI)

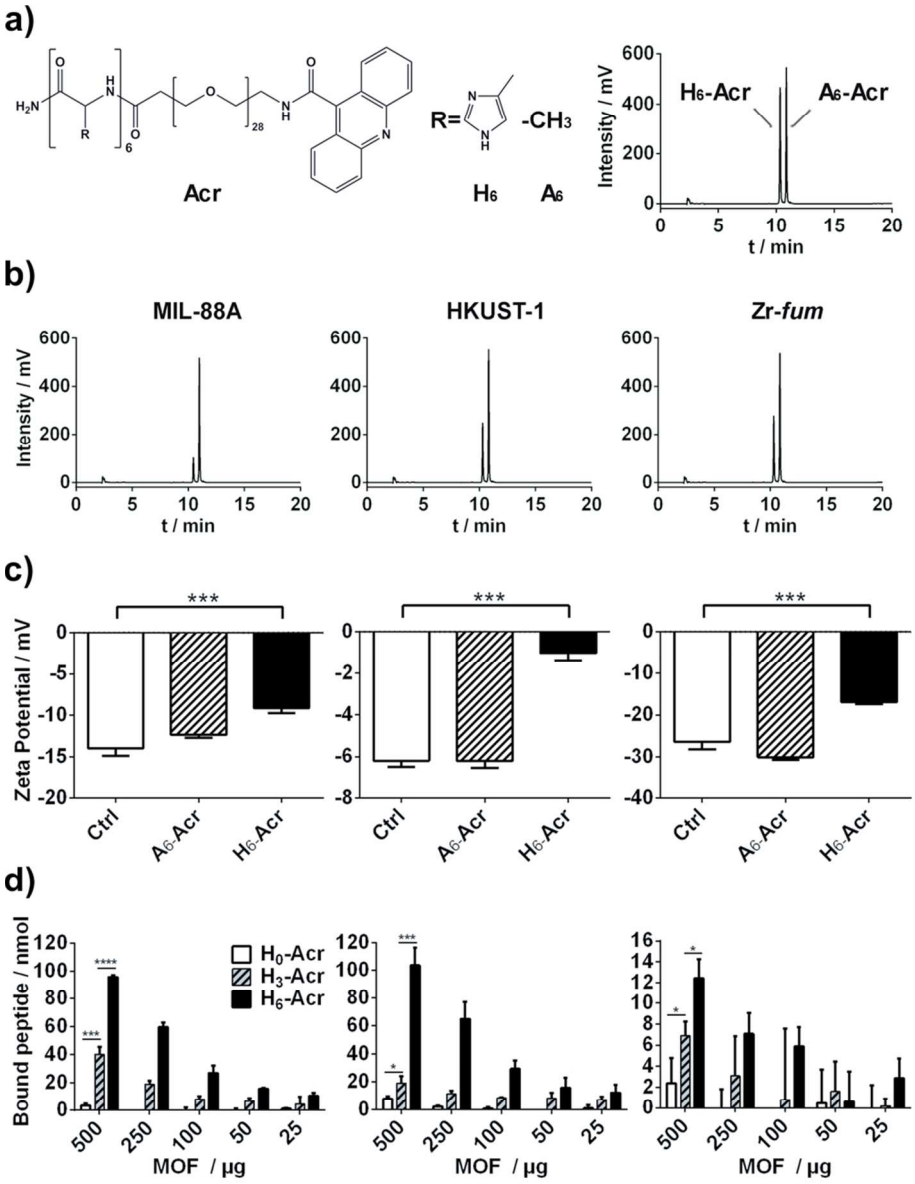

Figure 2. Acridine (Acr) peptide binding to MIL-88A (left), HKUST-1 (middle) and Zr-fum (right) particles in HEPES buffered glucose (HBG) at pH 7.4. a) Chemical structure and control chromatogram of model compounds H6-Acr, A6-Acr. b) Peptide binding (H6 vs. A6) by detection of reduced free peptides in the supernatant (RP-HPLC, λ=360 nm). c) Effect of peptide binding on zeta potential. d) Quantitative determination of bound peptides H0 (white), H3 (pattern), H6 (black) as difference to photometrically quantified free pep-tides in the supernatant (λ=360 nm) using a UV-photometer. Please note that the scaling of y-axes is accommodated to the different binding capacities: 0-120 nmol peptide in case of MIL-88A and HKUST-1, 0-16 nmol peptide in case of Zr-fum.

85x111mm (300 x 300 DPI)

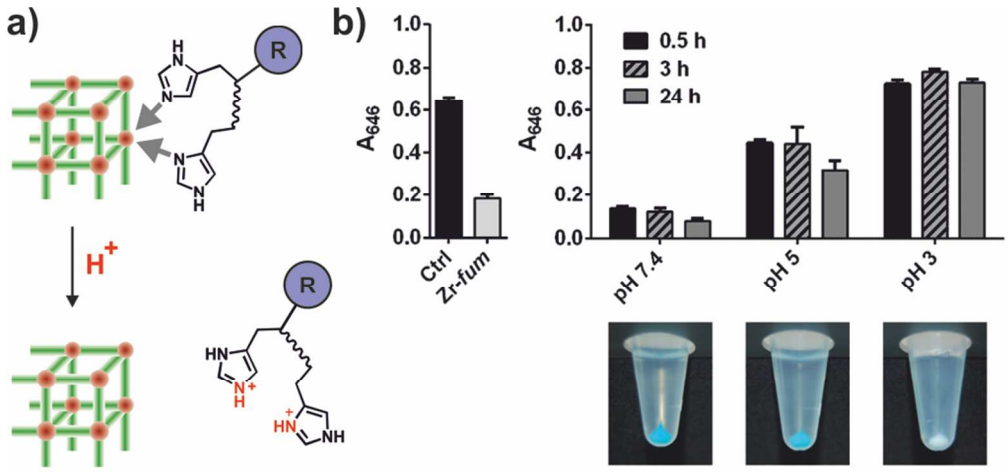

Figure 3. pH dependent stability of H6-tag binding to Zr-fum NPs. a) Schematic illustration of acidic detachment due to histidine protonation. b) Experimental data obtained by photometric determination (λ=646 nm) of free H6-A647N in the supernatant after centrifugation. Left: Zr-fum NPs were loaded with H6-A647N at pH 7.4 for 15 min, centrifuged and the supernatant was analyzed; Ctrl illustrates absorbance of free peptide in a sample without MOF NPs. Right: MOF NP suspensions were acidified to a defined pH and incubated for indicated times before centrifugation and analysis of the supernatant. Reaction tubes below show the MOF pellets of the same samples after 24 h at pH 7.4 (left), pH 5 (middle), pH 3 (right) and centrifugation; decoloration of the pellet due to acidic H6-A647N detachment at pH 3 can be observed.

86x39mm (300 x 300 DPI)

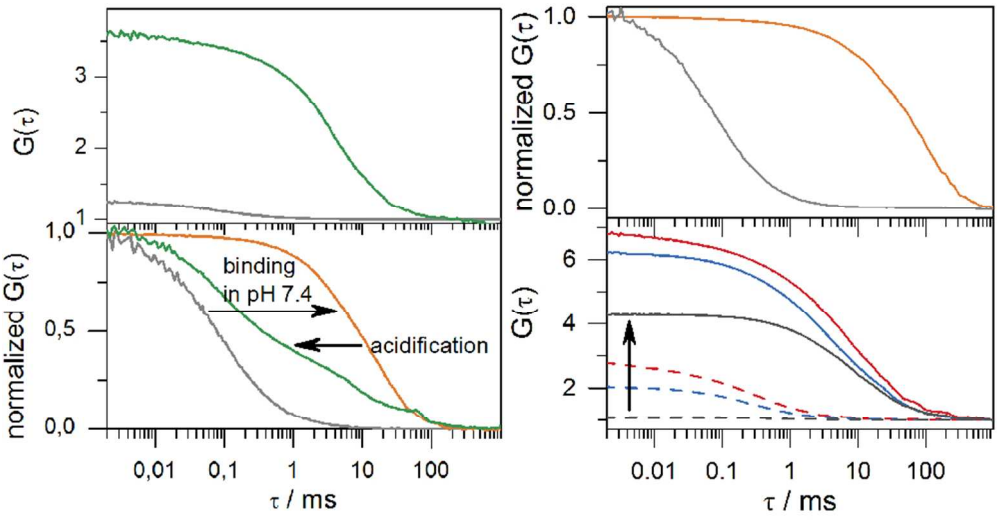

Figure 4. Investigation of Zr-fum/H6-A647N interaction by fluorescence correlation spectroscopy (FCS). Upper left: FCS time correlation functions of H6-A647N before (grey) and after Zr-fum NP addition (green). Lower left: Normalized time correlation functions of binding of H6-A647N at pH 7.4 (orange) and release upon acidification (green); free H6-A647N (grey). Upper right: Normalized time correlation functions of measurements in DMEM (10 % FBS) of free H6-A647N (grey) and Zr-fum/H6-A647N (orange). Lower right: fluorescence cross correlation spectroscopy (FCCS) measurements of H6-GFP (blue) and H6-Tf* (red) in HBG pH 7.4 before (dotted) and after (solid) Zr-fum addition. Cross correlation before (dotted grey) and after (solid grey) Zr-fum addition.

84x44mm (300 x 300 DPI)

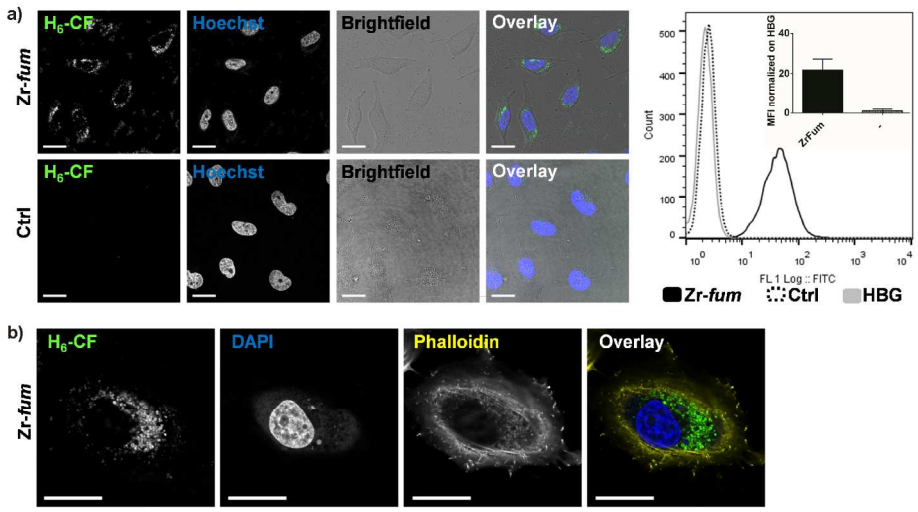

Figure 5. Cellular uptake of fluorescent peptide H6-CF mediated by Zr-fum NPs. H6-CF was incubated with Zr-fum MOF NPs for 15 min at room temperature in HBG for prefunctionalization by coordinative self-assembly. The functionalized particles were incubated with HeLa cells for 24 h at a concentration of 0.1 mg/mL Zr-fum corresponding to 1 µM H6-CF . Solutions containing H6-CF at same concentration but no Zr-fum NPs served as control (Ctrl). a) Confocal laser scanning microscopy (CLSM, left) and flow cytometry (right) after incubation of HeLa cells with functional NPs Zr-fum/H6-CF (Zr-fum, CLSM upper row, flow cytometry solid black), H6-CF control without Zr-fum NPs (Ctrl, CLSM lower row, flow cytometry dotted black) or HBG (flow cytometry grey). Mean fluorescence intensity (MFI) was normalized to HBG and is depicted in the inset. CLSM left to right: green fluorescence of H6-CF, nuclear staining with Hoechst dye, brightfield image, overlay of all three channels. b) Enlarged CLSM image of a fixated HeLa cell after incubation with Zr-fum/H6-CF. Left to right: green fluorescence of H6-CF, nuclear staining with DAPI dye, actin staining with rhodamine-phalloidin, overlay of all three channels. Scale bar: 25 µm. Additional images can be found in the Supporting Information Figure S23 and S24.

177x90mm (300 x 300 DPI)

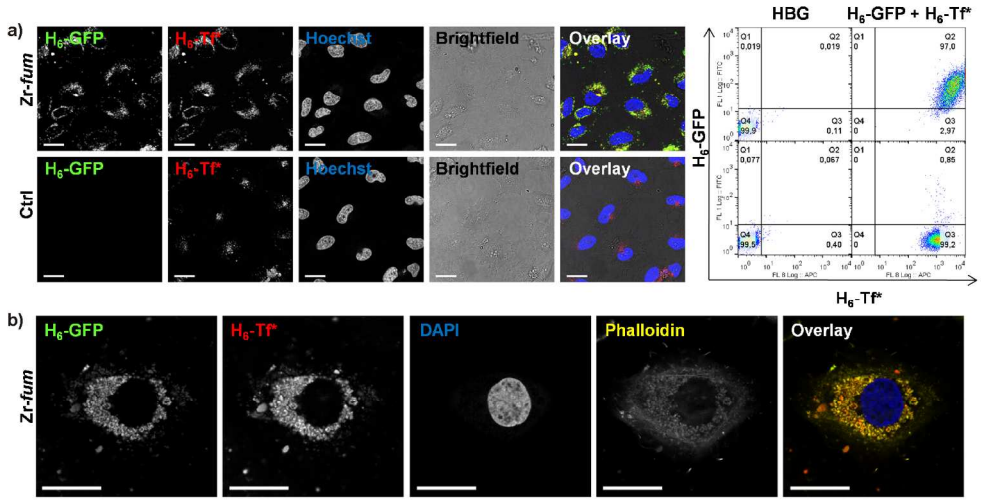

Figure 6. Simultaneous cellular uptake of fluorescent proteins H6-GFP and H6-Tf* mediated by Zr-fum NPs. An equimolar mixture of H6-GFP and H6-Tf* was incubated with Zr-fum MOF NPs for 15 min at room temperature in HBG for prefunctionalization by coordinative self-assembly. The double functionalized particles were incubated with HeLa cells for 24 h at a concentration of 0.1 mg/mL Zr-fum corresponding to 0.5 µM H6-GFP and H6-Tf*. Solutions containing H6-GFP and H6-Tf* at same concentration but no Zr-fum NPs served as control (Ctrl). a) Cellular uptake of Zr-fum/H6-GFP+H6-Tf* (upper row) or control without MOF NPs (lower row). CLSM left to right: green fluorescence of H6-GFP, red fluorescence of H6-Tf*, nuclear staining with Hoechst dye, brightfield picture, overlay of all four channels, yellow color indicates co-localization of H6-GFP and H6-Tf*. Flow cytometry analysis: HBG (left) or H6-GFP +H6-Tf* (right) with Zr-fum MOF NPs (upper row) or Ctrl without MOF NPs (lower row). b) Enlarged CLSM image of a fixated HeLa cell after incubation with Zr-fum/H6-GFP+H6-Tf*. Left to right: green fluorescence of H6-GFP, red fluorescence of H6-Tf*, nuclear staining with DAPI dye, actin staining with rhodamine-phalloidin, overlay of all four channels. Scale bar: 25 µm. Additional images can be found in the Supporting Information Figure S27 and S28 and a 3D reconstruction movie of a cell treated with Zr-fum/H6-GFP is provided as supporting material for download.

177x89mm (300 x 300 DPI)

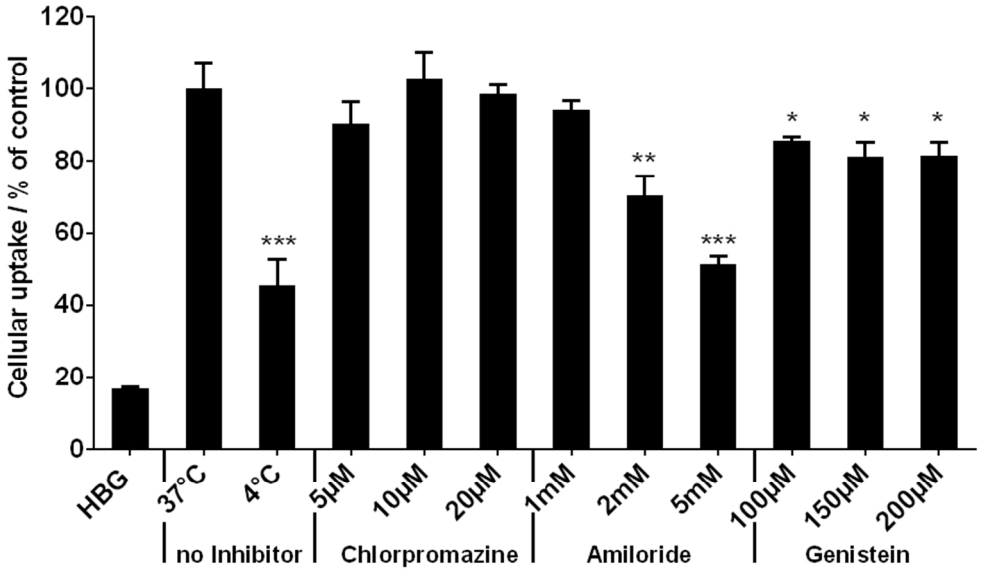

Figure 7. Evaluation of endocytosis inhibition of Zr-fum/H6-GFP nanoparticles. Pre-Incubation of HeLa cells with different inhibitors or at 4 °C for 30 min, followed by incubation with Zr-fum/H6-GFP for 2 h at 37 °C or 4 °C. Flow cytometric analysis was carried out in PBS (pH 4.0) to quench the extracellular fluorescence. Cellular uptake was determined as MFI. Data are presented as % cellular uptake normalized to uptake of Zr-fum/H6-GFP NPs at 37 °C ± SD (n=3).

80x48mm (300 x 300 DPI)

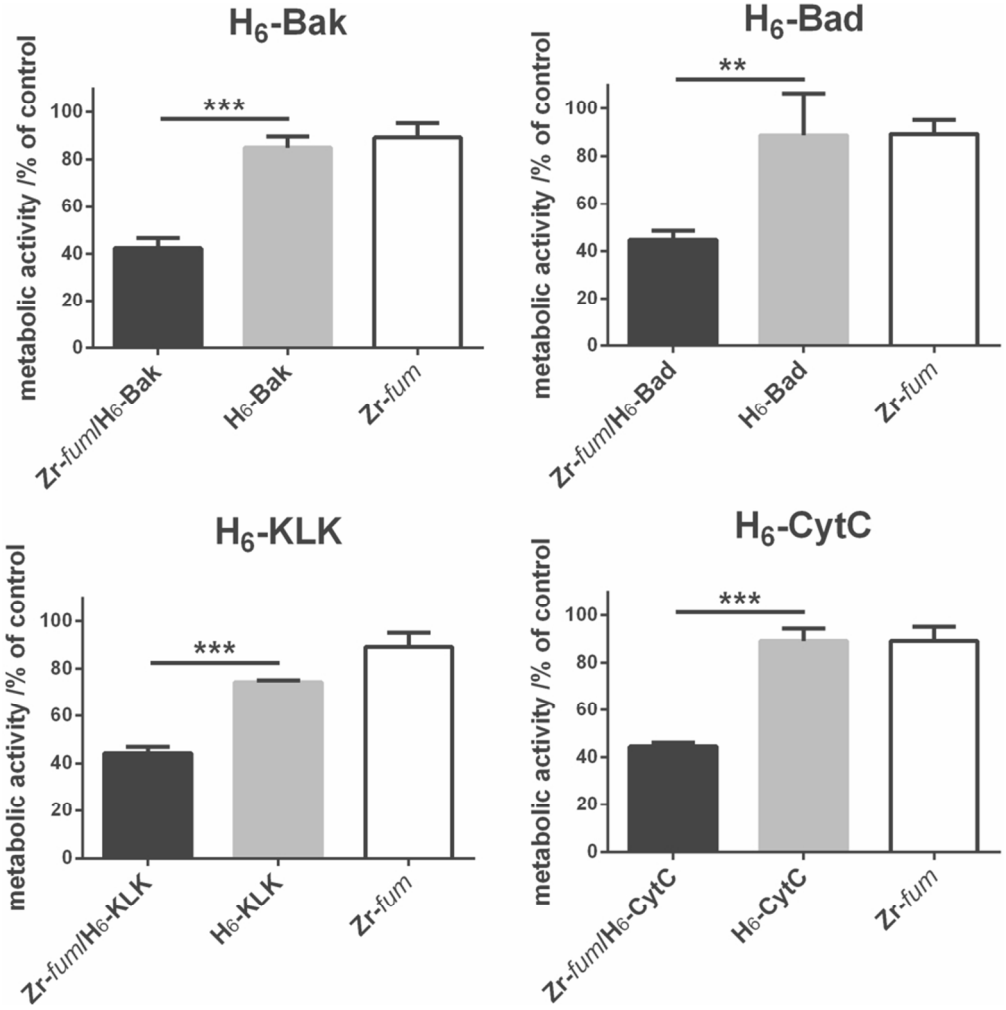

Figure 8. Intracellular transport of pro-apoptotic factors by Zr-fum MOF NPs and induction of HeLa cell killing upon incubation for 48 h. Final concentration of H6-Bak, H6-Bad, H6-KLK, H6-CytC was 10 µM (0.2 mg Zr-fum/10 nmol His-tag per mL medium). Data are presented as % metabolic activity of control cells ± SD (n=3) (MTT assay).

86x86mm (300 x 300 DPI)

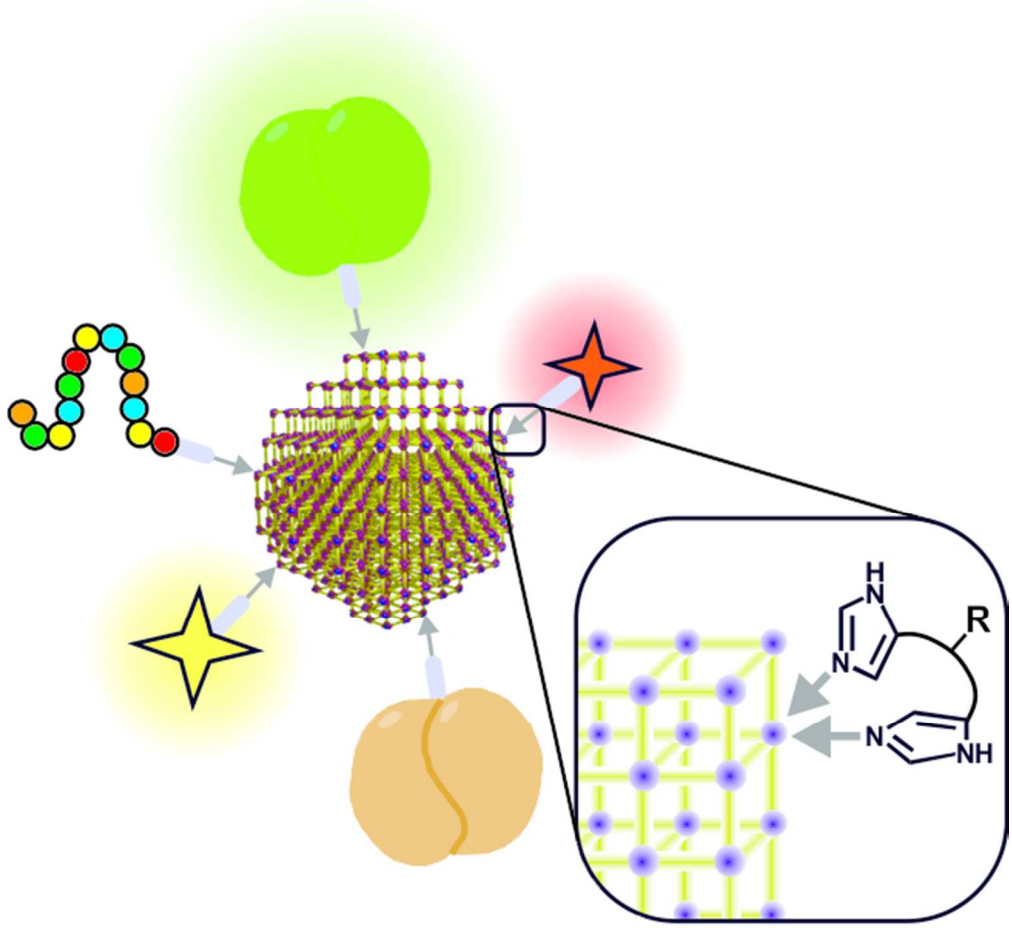

TOC Figure

55x51mm (300 x 300 DPI)